This is an open access article published under a Creative Commons Non-Commercial No Derivative Works (CC-BY-NC-ND) Attribution License, which permits copying and redistribution of the article, and creation of adaptations, all for non-commercial purposes.

CHEMISTRY OF MATERIALS
Cite This: Chem. Mater. 2019, 31, 5104−5115
Article
pubs.acs.org/cm

Edge-Site Nanoengineering of WS_2 by Low-Temperature Plasma-Enhanced Atomic Layer Deposition for Electrocatalytic Hydrogen Evolution

Shashank Balasubramanyam,[†] Mahdi Shirazi,[†] Matthew A. Bloodgood,[†] Longfei Wu,[‡] Marcel A. Verheijen,[†,§] Vincent Vandalon,[†] Wilhelmus M. M. Kessels,[†] Jan P. Hofmann,[‡] and Ageeth A. Bol*[,†]

[†]Department of Applied Physics and [‡]Laboratory for Inorganic Materials and Catalysis, Department of Chemical Engineering and Chemistry, Eindhoven University of Technology, 5600 MB Eindhoven, The Netherlands

[§]Eurofins Materials Science Netherlands B.V., High Tech Campus 11, 5656 AE Eindhoven, The Netherlands

Supporting Information

ABSTRACT: Edge-enriched transition metal dichalcogenides, such as WS_2, are promising electrocatalysts for sustainable production of H_2 through the electrochemical hydrogen evolution reaction (HER). The reliable and controlled growth of such edge-enriched electrocatalysts at low temperatures has, however, remained elusive. In this work, we demonstrate how plasma-enhanced atomic layer deposition (PEALD) can be used as a new approach to nanoengineer and enhance the HER performance of WS_2 by maximizing the density of reactive edge sites at a low temperature of 300 °C. By altering the plasma gas composition from H_2S to H_2 + H_2S during PEALD, we could precisely control the morphology and composition and, consequently, the edge-site density as well as chemistry in our WS_2 films. The precise control over edge-site density was verified by evaluating the number of exposed edge sites using electrochemical copper underpotential depositions. Subsequently, we demonstrate the HER performance of the edge-enriched WS_2 electrocatalyst, and a clear correlation among plasma conditions, edge-site density, and the HER performance is obtained. Additionally, using density functional theory calculations we provide insights and explain how the addition of H_2 to the H_2S plasma impacts the PEALD growth behavior and, consequently, the material properties, when compared to only H_2S plasma.

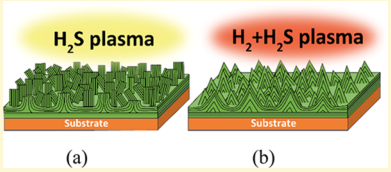

INTRODUCTION

Since the discovery of graphene, research on analogous, layered two-dimensional (2D) materials has garnered significant interest. In this regard, layered transition metal dichalcogenides (TMDs) have emerged as a promising class of materials due to their structural similarities with graphene and their unique thickness-dependent physicochemical properties.[1−3] Each layer in a TMD consists of hexagonally packed transition metal atoms that are sandwiched between two chalcogen atom layers.[2] The individual TMD layers are held together by weak van der Waals forces and can be exfoliated into monolayers.[2] Unique material properties emerge in these 2D nanoscale regimes that can deviate significantly from the bulk, due to quantum confinement effects.[2,4,5] Particularly, semiconducting TMDs such as MoS_2 and WS_2 exhibit an indirect band gap in their bulk form that transitions into a direct band gap in the monolayer (ML) regime.[6−9] In addition to the presence of a sizeable band gap, these semiconducting TMDs also exhibit a high carrier mobility, resulting in a high on/off ratio, which showcases their potential for future applications in electronic and opto-electronic devices.[10−12]

Interestingly, due to reduced atomic coordination, the edges of these layered TMD sheets exhibit different electronic,[13,14] optical,[15,16] and chemical[17,18] properties when compared to the basal planes. In 2005, theoretical studies identified MoS_2 as a biomimetic catalyst for the electrochemical hydrogen evolution reaction (HER) for water splitting due to the small Gibbs free energy for hydrogen adsorption on the reactive edges.[19] Subsequent experimental studies demonstrated that MoS_2 edges are indeed the active sites for HER, whereas the (00*l*) basal planes are catalytically inert.[20−22] Several studies have since reported the promising HER performance of MoS_2[23−25] and WS_2[26−28] electrocatalysts, further suggesting that these materials could be promising alternatives to noble metal catalysts such as Pt, the current benchmark HER electrocatalyst. Many of these studies focus on enhancing the edge-site densities to improve the HER performance;[26,29−31] however, research on this aspect is still ongoing. The density of the exposed edge sites depends on the morphology of the films, and the controlled synthesis of edge-enriched nanostructured catalysts is quite challenging.

Previously, edge-enriched MoS_2 and WS_2-based catalysts have been synthesized using chemical vapor deposition (CVD),[28,29,32] chemical exfoliation,[23,33,34] sulfurization of the metal or metal oxide using S or H_2S,[30,35,36] solvent-based chemical methods,[31,37−39] etc. To enhance the density of

Received: March 12, 2019
Revised: June 24, 2019
Published: June 25, 2019

© 2019 American Chemical Society

DOI: 10.1021/acs.chemmater.9b01008
Chem. Mater. 2019, 31, 5104−5115

exposed edge sites in the as-deposited material, edge-site engineering through ball milling,[26] strain[33,40] and defect induction,[41−43] basal plane activation,[40,44] postdeposition annealing,[37,45] vertically aligned layers,[30,31,46] etc., have also been examined. However, a reliable method to precisely control the edge-site density in these 2D materials has remained elusive, as concurred by Ho et al.[47] Conformal film growth on high-surface-area three-dimensional (3D) substrates and low-temperature processing (on temperature-sensitive substrates) are some of the other challenges that are yet to be addressed.

Recently, controlled growth of edge-enriched MoS_2[47,48] and WS_2[49] nanostructures with promising HER performance has been demonstrated using atomic layer deposition (ALD) at low growth temperatures (≤450 °C). ALD is typically a low-temperature (<500 °C) cyclic deposition technique characterized by saturated surface reactions of a precursor and a co-reactant.[50−52] The saturated, self-limiting reactions enable conformal film deposition on high-surface-area 3D structures/substrates that are typically employed for enhancing HER performance, which is otherwise a challenging endeavor with other synthesis techniques.[49,52,53] Furthermore, the use of plasma in one of the steps in an ALD cycle (so-called plasma-enhanced ALD) offers additional freedom in processing conditions that can influence material properties.[51,52,54] Therefore, ALD can be a promising synthesis route for the controlled growth of nanostructured 2D materials that are suitable for a variety of thin-film applications, including HER catalysts.

In the literature, there are very few reports on the low-temperature (≤450 °C), controlled growth of edge-enriched electrocatalysts for HER using ALD.[47−49] Ho et al. have reported the ALD growth of edge-enriched MoS_2 using a halide precursor ($MoCl_5$), in combination with H_2S as a co-reactant.[47] However, the film growth rate varied laterally across the growth surface (Au/Si, 4 in. wafer), hinting at the presence of a CVD component in their process. Deviation from the characteristic self-limiting ALD growth behavior hampers the inherent merits that ALD offers (thickness control, 3D conformality, uniform growth over large areas, etc.). Yeo et al. have reported the plasma-enhanced atomic layer deposition (PEALD) growth of WS_2 using a carbonyl precursor ($W(CO)_6$) and a H_2S plasma as a co-reactant on 3D, Ni-foam substrates.[49] However, there was no discussion on controlling the density of active sites. Sharma et al. demonstrated the temperature-dependent growth of "out-of-plane oriented (OoPO)" MoS_2 using a metalorganic precursor (bis(*tert*-butylimido)-bis(dimethylamido)-molybdenum) (chemical formula = $Mo(NMe_2)_2(N^tBu)_2$) and a H_2 + H_2S plasma mixture as a co-reactant.[48] These OoPO structures were predominantly edge-terminated, and the density of these structures could be controlled by varying the temperature.

In this work, we show that the material properties of WS_2 spanning the surface morphology, crystallinity, and stoichiometry can be tailored precisely by PEALD at 300 °C by altering the co-reactant plasma gas composition from H_2S to H_2 + H_2S. Hydrogen is known to be a strong reducing agent, and using density functional theory (DFT) calculations we describe how the addition of hydrogen to the H_2S plasma can influence the PEALD growth behavior and, consequently, change the material properties, when compared to only H_2S plasma. We demonstrate that controlling the plasma gas composition during PEALD of WS_2 provides a reliable method to tailor the morphology and composition and, consequently, the edge-site density and chemistry. The precise control over edge-site density was evaluated using electrochemical copper underpotential depositions (Cu-UPD), which has recently been reported by Voiry et al.[33] as a reliable technique to probe catalytically active edge sites of WS_2. Subsequently, the HER performance of the edge-enriched WS_2 electrocatalyst is demonstrated, and a clear correlation among plasma conditions, edge-site density, and the HER performance is obtained.

EXPERIMENTAL SECTION

PEALD of WS_2. WS_2 thin films were synthesized by PEALD in a commercial FlexAL ALD reactor from Oxford instruments. The reactor was equipped with an inductively coupled plasma (ICP) source, and the plasma power was fixed at 500 W for all depositions. A base pressure of 10^{-6} Torr was realized in the reaction chamber using a turbomolecular pump. The reaction chamber wall temperature was set to 150 °C, whereas the substrate table temperature was set to 300 °C. Using these settings, the substrate temperature was estimated to be ∼240 °C (using a thermocouple on reference samples), due to limited thermal contact in vacuum. Prior to deposition, the reaction chamber walls and substrate table were preconditioned with 500 ALD cycles (∼50 nm) of Al_2O_3 and 300 ALD cycles (∼25 nm) of WS_2. All substrates were subjected to a 20 min preheating step in a 200 mTorr Ar environment to stabilize the substrate temperature. Squares of crystalline silicon (*c*-Si) with 450 nm thick thermally grown SiO_2 on top (2 × 2 cm^2) (N-type doped, SIEGERT Wafer) and glassy carbon (2 × 2 cm^2, Goodfellow) were used as substrates. The glassy carbon substrates were polished with a 0.3 μm alumina suspension to obtain a mirror finish before use. The metalorganic precursor bis(*tert*-butylimido)-bis(dimethylamido)-tungsten (chemical formula = $W(NMe_2)_2(N^tBu)_2$) (99% purity, Sigma Aldrich) was used as the tungsten source. The precursor was stored in a canister heated to 50 °C and was bubbled into the reaction chamber through delivery lines heated to 70 °C. Ar (50 sccm flow) was used as the carrier gas to deliver precursor vapor from the canister to the reaction chamber.

Two PEALD processes were developed using the $W(NMe_2)_2(N^tBu)_2$ precursor with two plasma combinations as co-reactants: (1) H_2S plasma and (2) H_2 + H_2S plasma. The tungsten precursor used in this work was previously used to deposit WO_3 in a PEALD process over a wide temperature range from 100 to 400 °C, with little to no carbon impurity incorporation.[55] In the investigated temperature range, the precursor was found to be thermally stable without any signs of thermal decomposition. In this work, depositions were carried out at 300 °C as this was the lowest temperature at which the WS_2 films crystallized. During the co-reactant step, the H_2S and H_2 + H_2S gas delivery into the ICP source was always accompanied by Ar. For the H_2S + Ar plasma gas mixture, the respective flow rates into the ICP source were fixed at 10 sccm for H_2S and 40 sccm for Ar. For the H_2 + H_2S + Ar plasma gas mixture, the respective flow rates into the ICP source were fixed at 30 sccm for H_2, 2 sccm for H_2S, and 40 sccm for Ar. These particular flow rates were optimized after a series of experiments in which the flow rates of H_2S and H_2 gas were varied, and the impact of flow rate on the resulting surface morphology and crystallinity was studied. This is further described in detail in the Supporting Information (Figure S1).

Based on the saturation curves for precursor dosage (Figure S2a in the Supporting Information) and plasma exposure (Figure S2b), a WS_2 PEALD cycle with the following step sequence was adopted: 10 s precursor dosing, 10 s purge, 3 s pre-plasma time, 30 s plasma exposure, and 15 s purge. The pre-plasma time in the ALD cycle was utilized to stabilize the gas flows into the ICP source, and the plasma was ignited only during the subsequent plasma exposure step. The reaction chamber pressure was maintained at (1) 30 mTorr during precursor dosing and precursor purge steps and (2) 15 mTorr during plasma exposure and plasma purge steps.

DOI: 10.1021/acs.chemmater.9b01008
Chem. Mater. 2019, 31, 5104−5115

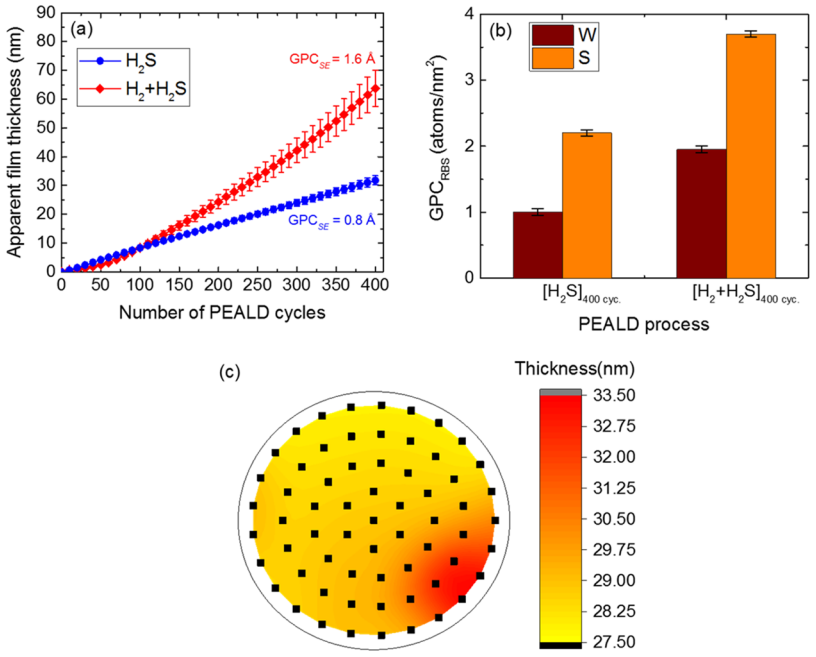

Figure 1. (a) Apparent film thickness (t_{App}) as a function of number of PEALD cycles for the H_2S and H_2 + H_2S processes at a deposition temperature of 300 °C, as determined from in situ SE measurements. The error bars are a cumulative sum of the measurement error and SE model fitting error. (b) GPC_{RBS} (atoms/nm^2) in terms of number of deposited W and S atoms showing an analogous trend as GPC_{SE} for the H_2S and H_2 + H_2S processes. GPC_{RBS} was determined after 400 PEALD cycles. (c) Thickness uniformity map of WS_2 films (H_2S process) on a 4 in. SiO_2/Si wafer, as determined from room-temperature ex situ SE measurements. The black squares on the wafer represent the SE measurement points with a 5 mm edge exclusion.

Material Characterization. For material characterization, WS_2 films grown on *c*-Si with 450 nm thermal oxide substrates were utilized, unless stated otherwise. The WS_2 apparent film thickness (t_{App}) was monitored in situ during PEALD using spectroscopic ellipsometry (SE). Ellipsometric spectra were recorded after every 10th PEALD cycle using a rotating compensator ellipsometer (M2000 U, J.A. Woollam, Inc.) over a spectral range of 1−5 eV. The measured ellipsometric data were fitted using a material model based on a B-spline function to determine the apparent film thickness. Due to the rough morphology of the 3D structures (especially in the case of the H_2 + H_2S process), the thickness could not be determined as accurately as on planar surfaces. However, the thickness values could be determined with an error margin and can be considered reliable within that error margin, as done in this work. Multiple in situ and ex situ SE measurements on a set of samples yielded very similar values, and the thickness determined by in situ SE was in good agreement with the thickness estimated from cross-section scanning transmission electron microscopy (STEM) images.

The absolute film composition, stoichiometry, and mass density were determined using Rutherford backscattering spectroscopy (RBS) and elastic recoil detection (ERD) measurements. The RBS and ERD measurements were performed by Detect 99 (Eindhoven, The Netherlands) using a 2000 keV He^+ beam. X-ray photoelectron spectroscopy (XPS) was also used to study the film composition. XPS studies were carried out using a Thermo Scientific KA1066 spectrometer with a monochromatic Al Kα X-ray source ($h\nu$ = 1486.6 eV); the XPS data processing was performed using the Avantage software. All elemental binding energies were calibrated with respect to the sp^3 carbon 1s peak at 284.8 eV. To study the microstructure of the films, high-angle annular dark field (HAADF) scanning transmission electron microscopy (STEM) images were taken on a probe-corrected JEOL JEM-ARM200F transmission electron microscope (TEM) operated at 200 kV. For top-view TEM studies, WS_2 was grown on Si_3N_4 windows coated with 5 nm of ALD SiO_2. For cross-section TEM studies, WS_2 films deposited on Si_3N_4 windows were coated with an additional SiO_2 protective layer, and a focused ion beam was used to create a cross-sectional sample. Further surface morphology studies were carried out by scanning electron microscopy (SEM) using a Zeiss Sigma microscope operated at 2 keV acceleration voltage. The crystallinity of the WS_2 films was studied using X-ray diffraction (XRD) measurements. XRD measurements were performed using a PANalytical X'Pert Pro MRD system using a Cu Kα X-ray source (λ = 1.54 Å). To obtain an overview of the reactive species present in the plasmas used in this work, optical emission spectroscopy (OES) was performed using a USB4000 spectrometer from OceanOptics.

Electrochemical Characterization. All electrochemical measurements were performed using a standard three-electrode cell set-up and an AUTOLAB potentiostat (model PGSTAT302N). A Pt wire and a saturated calomel electrode (Hg/Hg_2Cl_2 in saturated KCl) were used as the counter and reference electrodes, respectively. WS_2 films on glassy carbon substrates were used as the working electrodes. Prior to electrochemical measurements, the electrolyte was degassed with Ar for 15 min. WS_2 grown on glassy carbon was held in a circular poly(ether ether ketone) holder that exposed a working electrode area of 3.14 cm^2 to the electrolyte and was connected to a rotating disk. Linear sweep voltammetry (LSV) was performed at a scan rate of 50 mV/s in 100 mL of 0.5 M H_2SO_4 electrolyte. During LSV measurements, the working electrodes were rotated at 800 rpm. The Tafel slope was calculated by fitting the linear portion at the low-overpotential region to the Tafel equation using LSV curves corrected by uncompensated resistance (IR correction). Electrochemical impedance spectroscopy (EIS) was performed over a frequency range of 1 Hz to 100 kHz. Copper underpotential deposition (Cu-UPD) measurements were used to evaluate the number of active sites in the WS_2 films using the method described by Voiry et al. and Green et al.[33,56] WS_2 films grown on glassy carbon substrates were also utilized in Cu-UPD experiments. All Cu-UPD measurements were carried out in 0.1 M H_2SO_4 and 0.002 M $CuSO_4$ solution at a linear voltammetric scan rate of 50 mV/s. For background correction, charges obtained from the electrode in 0.1 M H_2SO_4 (cupric ions free) were subtracted from the charges obtained for Cu stripping.

Computational Details. To study the adsorption of precursor ($W(NMe_2)_2(N^tBu)_2$) on the growing WS_2 thin film surface in the

DOI: 10.1021/acs.chemmater.9b01008
Chem. Mater. 2019, 31, 5104−5115

Table 1. GPC_{RBS} and Film Composition of WS_2 Films (t_{App} ~ 32 nm) Grown Using H_2S and H_2 + H_2S PEALD Processes[a]

PEALD process	W (atom/(nm^2 cycle))	S/W	W (atom/nm^2)	S (atom/nm^2)	[H] atom %	mass density (g/cm^3)
H_2S	1.00 ± 0.05	2.2 ± 0.1	3.9×10^{16}	8.6×10^{16}	8.7 ± 0.5	5.4 ± 0.3
H_2 + H_2S	1.40 ± 0.05	1.8 ± 0.1	3.4×10^{16}	6.1×10^{16}	13.3 ± 0.7	4.5 ± 0.6

[a]The stoichiometry (S/W) and number of deposited W and S atoms/(nm^2 cycle) were deduced from RBS measurements, whereas the hydrogen content was determined from ERD measurements. The error in the measurement of absolute number of W and S atoms/nm^2 was 1 and 2%, respectively. The mass density was determined by combining the RBS results and in situ SE determined thickness.

steady-state regime, self-consistent DFT calculations in the generalized gradient approximations were employed. Here, the dimethylamido ligand and the *tert*-butylimido ligand are represented by X = $N(CH_3)_2$ and Y = $NC(CH_3)_3$, respectively. Reaction energies (ΔE) of the precursor adsorption were calculated in a 3D periodic model, using Vienna Ab initio Simulation package.[57] In these calculations, the electronic energies were approximated using the projector-augmented wave[58] description of atomic cores and the functional of Perdew, Burke, and Ernzerhof.[59] The plane wave cut-off energy was set to 600 eV. For W atoms $6s^25d^4$, S atoms $3s^23p^4$, N atoms $2s^22p^3$, C atoms $2s^22p^2$, and O atoms $2s^22p^4$ electrons were included as valence electrons. The self-consistent steps were converged to an energy difference of at least 10^{-4} eV. Geometries were optimized using the conjugate-gradient scheme without symmetry restraints or fixed atoms, to a convergence of energy gradients of less than 10^{-3} eV/Å. Since the magnetic properties are essential for an accurate description of the energetics and kinetics, all calculations were carried out spin-polarized. More computational details can be found in a previous work.[60]

In principle, the following ALD reactions are included: adsorption, protonation of ligands, desorption of the protonated ligands, densification, cooperative effects, and ligand exchange. A complete list of ALD reactions of the amide precursor can be found in previous studies.[60−62] In this study, we only looked at the adsorption energy of the W precursor and the consequence of ligand protonation on the adsorption of the W precursor.

Details on how we build the simulation boxes, the adsorption of the W precursor on the WS_2 basal plane ({001} facet), and consequences of proton transfer on the W precursor adsorption (complementary calculations) on the WS_2 edge structure ({010} facet) can be found in the Supporting Information.

RESULTS AND DISCUSSION

PEALD of WS_2. The growth behavior of WS_2 films during the H_2S and H_2 + H_2S PEALD processes was investigated using in situ SE at a deposition temperature of 300 °C. Figure 1a shows the apparent film thickness (t_{App}) as a function of the number of PEALD cycles for the H_2S and H_2 + H_2S processes. For the H_2S process (blue circles), the thickness increased linearly with the number of cycles exhibiting characteristic ALD growth behavior, and a growth per cycle (GPC_{SE}) of ~0.8 ± 0.05 Å was recorded after 400 cycles. For the H_2 + H_2S process (red diamonds), a drastic increase in thickness was observed after ~60 cycles, and a doubled GPC_{SE} value of ~1.6 ± 0.1 Å was recorded after 400 cycles. A similar GPC trend in terms of the deposited W and S atoms/nm^2 was observed from RBS measurements (Figure 1b). GPC_{RBS} was determined by dividing the total number of deposited W or S atoms/nm^2 by the total number of ALD cycles. After 400 cycles, the GPC_{RBS} in terms of the W atoms deposited/nm^2 was determined to be ~1.00 ± 0.05 for the H_2S process and ~1.95 ± 0.05 for the H_2 + H_2S process, in line with the trend observed by GPC_{SE}. Film growth was observed right after the very first ALD cycle on the starting surface for both processes (Figure 1a) and repeated depositions yielded similar "thickness versus number of ALD cycles" profiles, indicating the high reproducibility of both PEALD processes. The GPC_{SE} saturation for precursor dosing and plasma exposure time, which confirm self-limiting ALD growth, are discussed in the Supporting Information (Figure S2). No film growth was observed with the thermal ALD variant using the same precursor used in this work in combination with H_2S gas (investigated for 200 ALD cycles). Plasma activation is required for growth to ensue.

Large-area, uniform film growth is very important from an application point of view, and ALD ideally yields uniform film growth over large-area substrates due to its self-limiting growth behavior.[52,53,63,64] To investigate this aspect, the WS_2 thickness uniformity on a 4 in. SiO_2/Si wafer was analyzed using room-temperature ex situ SE measurements, as shown in Figure 1c. A WS_2 film deposited with 400 ALD cycles using the H_2S process was utilized for the uniformity check. Over the mapped area, a small variation in WS_2 thickness was observed with a thickness nonuniformity of ~4% (nonuniformity = std. deviation/avg.). This indicated good thickness uniformity and the feasibility of this WS_2 PEALD process for growth on large-area substrates.

The material properties of the WS_2 films were studied next. Films with comparable thicknesses were deposited for an accurate comparison (t_{App} ~ 32 nm). Following the established GPC values for both processes (Figure 1a), 400 cycles were required for the H_2S process, whereas 240 cycles were sufficient for the H_2 + H_2S process to produce t_{App} ~ 32 nm films. Comparing the chemical composition of WS_2 films deduced from RBS measurements (Table 1), the H_2S process yielded a sulfur-rich film (S/W = 2.2), whereas a sulfur-deficient film (S/W = 1.8) was obtained from the H_2 + H_2S process (see also Table S1 for S/W ratios determined via XPS). The tungsten W 4f core-level spectrum acquired from XPS measurements is shown in Figure S3 in the Supporting Information. For the H_2S process, the characteristic doublet peaks W $4f_{7/2}$ and W $4f_{5/2}$ were observed at binding energies of 32.5 and 34.6 eV, respectively, suggesting a W^{4+} oxidation state. Slight peak shifts (~0.5 eV) toward higher binding energies were observed for the sulfur-deficient H_2 + H_2S process (S/W = 1.8), which could be due to the filling of sulfur vacancies with oxygen as a consequence of exposure to air prior to XPS measurements. For both processes, carbon, oxygen, and nitrogen impurities were observed only on the surface and not in the bulk of the films, as revealed by depth profiling with Ar ions (Figure S3). This indicated the growth of relatively pure tungsten disulfide films.

The number of deposited W and S atoms/nm^2 (per geometric area) were higher for the H_2S process. The mass density (Table 1) was also found to be higher for the film grown using the H_2S process (5.4 ± 0.3 g/cm^3) when compared with the H_2 + H_2S process (4.5 ± 0.6 g/cm^3). However, as observed in Figure 1a, the GPC_{SE} was higher for the H_2 + H_2S process, which was also in agreement with the GPC_{RBS} in Table 1. This implies that the growth behavior was different for the H_2 + H_2S process and will be discussed in morphological terms later in this article.

DOI: 10.1021/acs.chemmater.9b01008
Chem. Mater. 2019, 31, 5104−5115

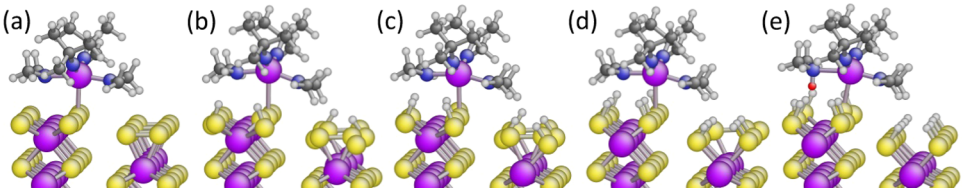

Figure 2. Chemical adsorption of WX_2Y_2 on the WS_2{010} facet at different H coverages, including vdW interactions. (a)−(e) correspond to reactions 1−5 in Table 2 depicting only final configurations. The increase of H coverage makes the precursor adsorption less favorable. However, proton transfer from the surface to the dimethylamido ligand (e) makes the precursor adsorption more favorable. Color coding in the figure: violet = W, yellow = S, dark blue = N, white = H, dark gray = C, and red = transferred proton. The dimethylamido ligand and the *tert*-butylimido ligand are represented as X = $N(CH_3)_2$ and Y = $NC(CH_3)_3$, respectively.

Table 2. Adsorption Energies (ΔE) of the W Precursor with and without vdW Interactions for Different −SH Coverages on the {010} WS_2 Facet[a]

	reaction	−SH coverage	ΔE (eV)	ΔE (eV) including vdW
1	$WX_2Y_2(g) \rightarrow WX_2Y_2(s)$	2 ML S and 0 ML H	−0.74	−0.54
2	$WX_2Y_2(g) \rightarrow WX_2Y_2(s)$	2 ML S and 0.5 ML H	−0.48	−0.80
3	$WX_2Y_2(g) + S(s) \rightarrow WX_2Y_2(s) + S(s)$	2 ML S and 1.0 ML H	−0.32	−0.59
4	$WX_2Y_2(g) + S(s) \rightarrow WX_2Y_2(s) + S(s)$	2 ML S and 1.5 ML H	−0.07	−0.29
5	$WX_2Y_2(g) + SH(s) \rightarrow WHX_2Y_2(s) + S(s)$	2 ML S and 2 ML H	0.37	−1.05
6	$WX_2Y_2(g) + SH(s) \rightarrow WHX_2Y_2(s) + S(s)$	2 ML S and 1.0 ML H	−0.28	−1.95
7	$WX_2Y_2(g) + SH(s) \rightarrow WHX_2Y_2(s) + S(s)$	2 ML S and 1.5 ML H	0.03	−1.47
8	$WX_2Y_2(g) \rightarrow WX_2Y_2$[b]	1.75 ML S and 1.5 ML H	0.21	−0.72
9	$WX_2Y_2(g) \rightarrow WX_2Y_2$[b]	1.5 ML S and 1.0 ML H	−0.07	−0.12
10	$WX_2Y_2(g) \rightarrow WX_2Y_2$[b]	1.25 ML S and 0.5 ML H	−0.25	−0.99
11	$WX_2Y_2(g) \rightarrow WX_2Y_2$[b]	1 ML S and 0 ML H	−0.55	−1.07

[a]The dimethylamido ligand and the *tert*-butylimido ligands are shown by X = $N(CH_3)_2$ and Y = $NC(CH_3)_3$, respectively. [b]Indicates the physisorbed precursor and ML = monolayer.

Hydrogen was observed in the WS_2 films obtained from both PEALD processes with the $H_2 + H_2S$ process exhibiting a higher hydrogen content (Table 1). Hydrogen species generated during the dissociation of the gas mixtures in the plasma can contribute to the observed hydrogen content in the WS_2 films. Apart from the plasma, the H content in the films may emanate from the ligands of the precursor (a single precursor molecule has 30 H atoms), residual water in the PEALD reactor, and/or from exposure to the ambient environment. From the plasma gas composition, one can expect a higher H content in the hydrogen-diluted $H_2 + H_2S$ plasma when compared to only H_2S plasma. The higher H content in the hydrogen-diluted $H_2 + H_2S$ plasma is validated when comparing the atomic H emission line intensities of both plasmas from OES data (Figure S4). The abundantly available H in the H_2-diluted H_2S plasma can scavenge S from the film growth surface, as H is known to be a strong reducing agent, and can explain the growth of sub-stoichiometric films in the case of the $H_2 + H_2S$ process (Table 1).

Computational Results. The ALD growth behavior is strongly influenced by the adsorption rate of the precursor on the growth surface. The abundantly available hydrogen in the $H_2 + H_2S$ plasma not only scavenges S atoms (Table 1) but can also modify the −SH surface coverage, which can significantly impact the precursor−surface interaction. To further understand the impact of these two effects on the growth behavior, DFT calculations were performed to investigate the precursor adsorption on two different crystalline facets of WS_2 containing S deficiencies and different −SH coverages. The precursor adsorption on both the WS_2 basal plane ({001} facet) and edge structure ({010} facet) is discussed. Here, we show the main results, and for further details, the reader is referred to the computational section in the Supporting Information.

Precursor Adsorption on WS_2 Basal Planes ({001} Facet). Different −SH coverages were considered to simulate the abundantly adsorbed H atoms and S deficiencies in the WS_2 layers (Table S2). The introduction of the W precursor to the WS_2 basal planes ({001} facet) with varying −SH coverage did not lead to strong precursor adsorption (Table S2, reactions 1−5). The introduction of precursor to the S atoms only led to the physisorption of the precursor, which was not energetically favorable (Figure S6a,b). Similarly, the introduction of precursor to W atoms resulted in the precursor being physisorbed (Figure S6c,d). Under specific conditions, the precursor chemisorbed on the surface, and the reaction became exothermic when the adsorbed H was accessible to the precursor ligands (Table S2, reaction 5). This could be considered as a seed precursor for the nucleation on the basal planes and, consequently, formation of a new layer (Figure S6e). For further details regarding the precursor adsorption on the basal plane, the reader is referred to the computational section in the Supporting Information.

Precursor Adsorption on WS_2 Edges ({010} Facet). The W precursor adsorption on the WS_2 edge structure ({010} facet) was studied next (Figure 2). Due to the under-coordination of the S atoms at the edges, the edges are known to be very reactive when compared to the S atoms at the basal planes.[2,18] Thus, the precursor adsorption on WS_2 edges ({010} facet) was expected to be much stronger than that on the basal planes ({001} facet). To investigate the consequence of the abundantly adsorbed H atoms on the WS_2 edge structure, different H coverages were considered, while maintaining a full S coverage (2 ML S) (Table 2, reactions 1−5). In each

DOI: 10.1021/acs.chemmater.9b01008
Chem. Mater. 2019, 31, 5104−5115

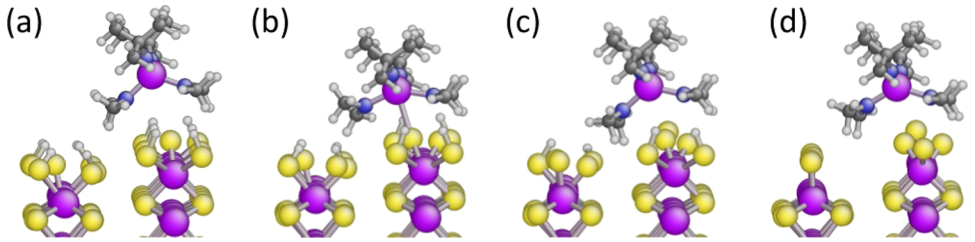

Figure 3. Physical adsorption of WX_2Y_2 on the $WS_2\{010\}$ facet at different −SH coverages, including vdW interactions. The surface is reduced from (a) to (d) by desorption of a H_2S molecule creating different −SH coverages. The reduction of the $WS_2\{010\}$ surface makes precursor adsorption more favorable. This schematic corresponds to reactions 8−11 in Table 2. The color code and ligand abbreviations are the same as in Figure 2.

calculation, the W precursor was introduced to the same S atom at the edge structure. On these edge structures, the introduction of H atoms breaks the bonds between neighboring S atoms (Figure 2a−e), resulting in varying degrees of −SH termination. Our simulations indicate that the precursor adsorption energy (ΔE) increases from −0.74 to 0.37 eV with increasing −SH coverage implying a weaker adsorption with increased H coverage (reactions 1−5 in Table 2).

A similar trend was observed upon the inclusion of vdW interactions with increasing −SH coverage. Interestingly, however, ΔE became exothermic by 1.05 eV implying a stronger precursor adsorption at full H coverage (Figure 2e and reaction 5, Table 2). This change was due to a proton transfer from the surface to the dimethylamido ligand (X) of the precursor (red sphere in Figure 2e) and was further investigated.

The consequence of proton transfer on the adsorption of the W precursor was investigated by considering two H coverages of 1.0 ML and 1.5 ML (Table 2, reactions 6 and 7). For these studies, H atoms were relocated at the surface to be accessible to the N atom of the dimethylamido ligand.[60,61] It was observed that the proton transfer from the surface −SH group to the dimethylamido ligand occurs during the optimization (Figure S7), leading to a reduction in the overall system energy. Hence, proton transfer is effectively barrierless. Upon the inclusion of vdW interactions, the proton transfer made a significant difference in the adsorption energy. At a 1.0 ML H coverage, the adsorption energy was exothermic by 1.95 eV (Table 2, reaction 6), which was more favorable than the same adsorption in the absence of proton transfer by 1.36 eV (ΔE = −0.59 eV, Table 2, reaction 3). A similar trend was observed at a higher H coverage of 1.5 ML (Table 2, reaction 7). This clearly indicated that the precursor adsorption is strongly promoted by increased H coverage upon inclusion of vdW interactions.

Proton transfer in the absence of vdW interaction did not make a large difference in the adsorption energy ($\Delta E \leq 0.1$ eV). Proton transfer to the dimethylamido ligand gave rise to the chemical adsorption of the W precursor, whereas the absence of proton transfer to the W precursor resulted in only physical adsorption at the surface (Figure S8).

To investigate the consequence of removal/etching of S atoms from the WS_2 edge structure, one S and two H atoms were randomly removed from the $WS_2\{010\}$ surface with a full −SH coverage. The removed atoms were considered as a desorbed H_2S molecule (Figure 3). After desorption of H_2S, surface reconstruction ensued with S atom relocation, effectively minimizing the surface energy (Figure S9). Reactions 8−11 in Table 2 reveal an exothermic precursor adsorption with decreased −SH coverage, implying that the reduction of the WS_2 surface (by removal of S atoms) also makes precursor adsorption more favorable.

To summarize, DFT calculations confirm that the W precursor adsorption at the edge structure ({010} facet) is strongly promoted by increased H coverage and S deficiency. A higher precursor adsorption rate translates into a higher GPC. The higher GPC observed previously for the H_2 + H_2S process (Figure 1a and b) can be explained by such an enhanced precursor adsorption.

Crystallinity and Morphology. To evaluate the crystallinity of the as-grown WS_2 films (t_{App} ∼ 32 nm), gonio-XRD measurements ($\theta - 2\theta$) were performed, and the corresponding diffraction patterns are shown in Figure 4a. The XRD peaks

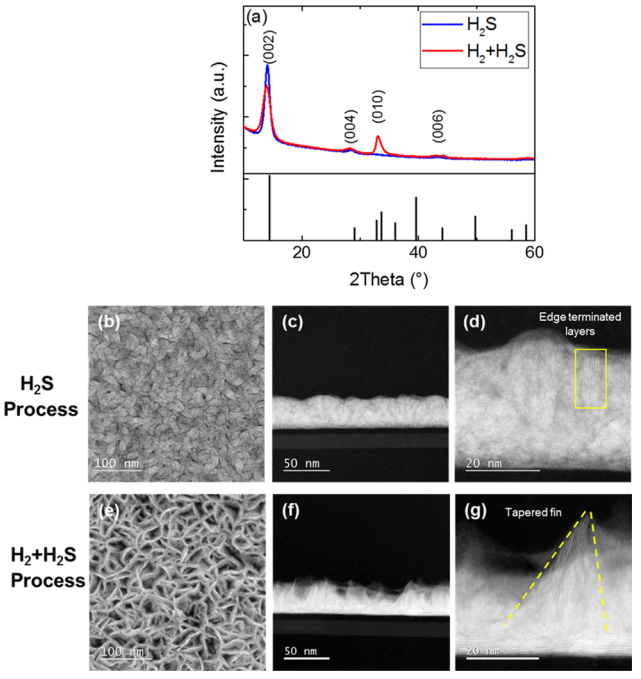

Figure 4. (a) Gonio-XRD patterns of WS_2 films (t_{App} ∼ 32 nm) grown using H_2S and H_2 + H_2S PEALD processes. The powder diffractogram of 2*H*-WS_2 is included as a reference[65] and is represented by vertical bars at the bottom of the figure. (b−g) HAADF-STEM images of edge-enriched WS_2 films (t_{App} ∼ 32 nm): (b) Top-view and (c, d) cross-sectional images of WS_2 grown using the H_2S process. The edge termination of the WS_2 layers is highlighted with a rectangle in (d). (e) Top-view and (f, g) cross-sectional images of WS_2 grown using the H_2 + H_2S process. Dashed lines follow the triangular-fin outline in (g).

DOI: 10.1021/acs.chemmater.9b01008
Chem. Mater. 2019, 31, 5104−5115

corresponding to hexagonal 2*H*-WS_2 were observed, which confirmed the growth of crystalline films at a very low deposition temperature of 300 °C for both PEALD processes. The H_2S process exhibited a relatively intense (002) peak, indicating the growth of crystalline WS_2 with a preferential orientation of the (00*l*) series. The H_2 + H_2S process also exhibited an intense (002) peak, as well as a peak corresponding to the (010) plane, suggesting the growth of crystalline WS_2 with significant contributions from two different preferential orientations. Based on these observations, we can conclude that tuning the plasma gas composition enables the growth of WS_2 layers with varied orientations and allows for controlling the texture of nanostructured WS_2 during PEALD.

We studied the morphology of the WS_2 films using HAADF-STEM to obtain further insights about the ALD growth behavior. The top-view and cross-sectional STEM images in Figure 4b−g show morphological differences in the WS_2 films (t_{App} ∼ 32 nm). WS_2 grown using the H_2S process (Figure 4b) yielded densely packed "nanoflakes" with individual lateral flake sizes ranging from ∼10 to 20 nm. In stark contrast, the H_2 + H_2S process led to the growth of high surface area open structures (Figure 4e). For the H_2S process, cross-sectional STEM images (Figure 4c,d) revealed that the initial few layers of WS_2 grew in a two-dimensional (2D) laterally oriented fashion on the substrate. Upon increasing the film thickness beyond a few layers, a change in the growth direction was observed, with the layers now forming three-dimensional (3D) features at oblique angles with the surface normal. The edges of these obliquely oriented, dense layers appeared to predominantly terminate on the top surface (Figure 4d). In contrast, for the H_2 + H_2S process (Figure 4f,g), after the growth of a few initial 2D horizontal layers of WS_2 on the starting surface, subsequent layers started to form 3D fin-like triangular structures with their edges tapering toward the top surface (Figure 4g). For these films, the apparent thickness can be interpreted as the average value of film thickness from the growth surface (substrate) to the peak.

A growth model was postulated by Sharma et al. to explain the morphological transition from 2D horizontal basal planes to 3D structures as a function of the number of cycles in PEALD-grown MoS_2.[48] This model can also be adopted to explain the morphology transition in our WS_2 films grown using both H_2S and H_2 + H_2S processes, owing to the similarities between the MoS_2 and WS_2 material systems and the PEALD processes used. According to this model, the initial film growth starts with the formation of islands with basal planes oriented parallel to the substrate. The growth at the edges of these islands is faster than growth on top of the basal planes due to the higher reactivity of edges. This aspect is well supported by the DFT results obtained in our work. Next, with increasing cycle number, competition between laterally expanding islands (2D planes) leads to defect-mediated growth at the grain boundaries, forcing the layers to grow in out-of-plane orientations (3D structures) at those boundaries. After this transition in morphology (2D to 3D growth), subsequent film growth results in the steady-state film morphology depicted in Figure 4.

Furthermore, based on RBS measurements (Table 1), we observed that the H_2 + H_2S plasma leads to the formation of S-deficient films. DFT calculations revealed that the removal of S atoms from the WS_2 film leads to a lower S coverage at edge sites (Figure S9 in the Supporting Information). Consequently, lower S coverage at the edges leads to weaker densification of the W precursor than in the case of complete S coverage.[60,61] Growth on such low-coverage surfaces can strongly influence the resulting material properties including crystallinity and morphology, as observed in the case of the H_2 + H_2S process. The lower S coverage can induce the migration of surface S atoms to reduce the surface energy (Figure S9) and lead to film growth along new crystal planes, as confirmed from XRD measurements (Figure 4a). This may explain the formation of the observed fin-like 3D structures in Figure 4f,g.

The increase in GPC after ∼60 cycles observed in Figure 1a for the H_2 + H_2S process can now be attributed to this change in the surface morphology from horizontal basal planes to vertical triangular-fin-like 3D structures. The fin-like structures with high surface area expose a significantly higher number of edge sites than the horizontal basal planes. The adsorption of the W precursor is enhanced on such edge sites ({010} crystal facet), as observed earlier from DFT calculations, and therefore, leads to an increase in the GPC, as seen in Figure 1a. The enhanced precursor adsorption for the H_2 + H_2S process (S-deficient and higher H coverage) can be confirmed by a relatively higher number of deposited W atoms/(nm^2 cycle) for the H_2 + H_2S process (1.4 ± 0.05) when compared to the H_2S process (S-rich and lower H coverage) (1 ± 0.05), as deduced previously from RBS measurements (Table 1). Furthermore, upon doubling the WS_2 film thickness to ∼64 nm for the H_2 + H_2S process, the number of deposited W atoms/(nm^2 cycle), and the density of the films and the density of triangular fins increased (Table S3 and Figure S10). However, the absolute number of W and S atoms per geometric area (nm^2) was observed to be lower for the H_2 + H_2S process, as discussed in Table 1. This indicates that the WS_2 films grown using the H_2 + H_2S process have less material per unit area than those grown using the H_2S process, which is corroborated by the open, triangular-fin-like 3D structures, as observed in Figure 4f,g. Although a change in surface morphology was observed also for the H_2S process, no drastic increase in GPC was observed in Figure 1a. The densely packed nanoflake-like structures formed after the morphology transition seem to offer a lower number of sites for precursor adsorption due to their lower surface area, when compared to the triangular-fin-like structures obtained with the H_2 + H_2S process. Thus, no drastic change in GPC is observed in Figure 1a.

Evaluation of Number of HER-Active Edge Sites. The HER performance of TMDs such as WS_2 is significantly dependent on the density of exposed edge sites. Above, we showed that the morphology of the WS_2 films could be modulated by varying the plasma gas composition (Figure 4b−g). As a consequence of their contrasting surface morphologies, WS_2 films synthesized in this work using the H_2S and H_2 + H_2S PEALD processes appeared to exhibit different edge densities on the surface (Figure 4b−g). Since the edges are the active sites for HER, a higher density of the exposed edge sites is expected to lead to a better HER performance. There are many reports in the literature that focus on increasing the density of exposed edge sites, but only a few have actually made an attempt to evaluate their numbers.[33,66,67] The electrochemical performance of a TMD electrocatalyst is dependent upon several factors, such as the number of exposed active sites, hydrogen binding energy, degree of crystallinity, charge transfer resistance, etc. Therefore, an evaluation of the number of exposed active sites can provide additional insights

DOI: 10.1021/acs.chemmater.9b01008
Chem. Mater. 2019, 31, 5104−5115

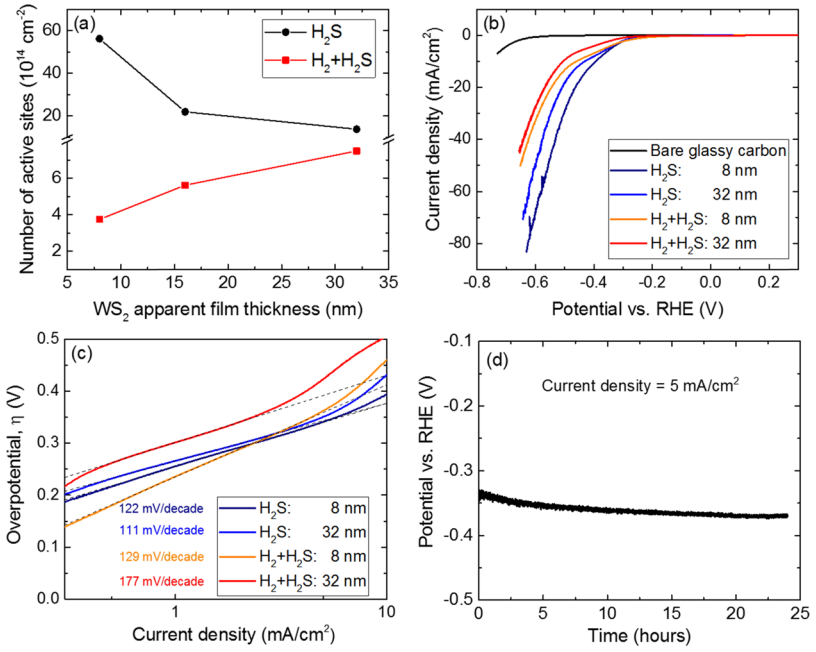

Figure 5. (a) Number of active sites per geometric area (cm^2) determined from Cu-UPD measurements for WS_2 films with various thicknesses (t_{App}) grown using the H_2S and H_2 + H_2S PEALD processes. (b) IR-corrected cathodic polarization curves (LSV) and (c) corresponding Tafel plots. (d) Stability of the overpotential required to reach a current density of 5 mA/cm^2 (η_5) for over 25 h of the WS_2 electrocatalyst (~8 nm) synthesized using the H_2S process.

toward understanding and provide opportunities to enhance the HER performance. Benck et al. and Shin et al. estimated the number of active sites from the electrochemically active surface area (determined using electrochemical capacitance measurements) in combination with a model based on the surface structure, which assumes a flat MoS_2 surface with negligible surface roughness.[66,67] This approach takes into account several assumptions and is not convenient for crystalline films with nanostructured morphology, which do not have atomically flat surfaces.

Taking a cue from Green et al.,[56] who utilized the Cu-UPD technique to determine the surface area of Pt and Ru in Pt−Ru electrocatalysts, Voiry et al. used Cu-UPD to estimate the number of active sites in strained, chemically exfoliated WS_2 nanosheets.[33] Using this technique, it is experimentally possible to estimate the number of active sites by comparing the charge of hydrogen adsorption and copper deposition at underpotential regions.[33] Cu-UPD has also been used by Zhang et al.[68] to evaluate the number of active sites in lithium-incorporated palladium phosphosulfide. In this work, we used Cu-UPD to evaluate the number of active sites per geometric area (cm^2) of PEALD WS_2 films using the method described by Voiry et al. and Green et al.[33,56] Details regarding the evaluation of the number of active sites from the Cu-UPD measurements are discussed in the Supporting Information (Figure S11). Glassy carbon substrates were used for Cu-UPD measurements, and through SEM (Figure S12), it was confirmed that the morphology of the WS_2 films grown on glassy carbon substrates was consistent with that of the WS_2 films grown on SiO_2 (450 nm)/Si substrates.

Figure 5a shows the number of exposed active sites per geometric area (cm^2) for the WS_2 films, as determined from Cu-UPD measurements. An order of magnitude difference was found between the PEALD processes irrespective of the film thickness: 10^{15} sites/cm^2 for the H_2S process and 10^{14} sites/cm^2 for the H_2 + H_2S process. This significant difference in the number of exposed active sites can be attributed to the differences in surface morphology and density of the respective WS_2 films (Figure 4b−g, Table 1).

The predominantly edge-terminated and more dense WS_2 films from the H_2S process contribute to a higher density of active sites per geometric area than the lower density, tapered-fin structures (reduced in both thickness and density at the top surface) in the H_2 + H_2S process. Although the surface area is greater in the case of the H_2 + H_2S process (Figure 4), the fin tapering leads to lower exposure of active edges on the top surface. Other than morphology and film density, the stoichiometry can also influence the number of active sites. The Cu-UPD process on S-rich (H_2S process) and S-deficient (H_2 + H_2S process) WS_2 surfaces can be quite different. From the Cu-UPD cyclic voltammograms in Figure S11, it was observed that the underpotential regions for the H_2S and H_2 + H_2S processes have similar potentials. So the relative comparison of the number of sites between the two processes can be treated as qualitatively fair.

For the H_2 + H_2S process in particular, an increase in film thickness from ~8 to ~32 nm resulted in an increase in the number of active sites/cm^2 from ~3.7 × 10^{14} to 7.5 × 10^{14} (Figure 5a). With increasing thickness, the film density increases as more WS_2 layers are added to the open structures, which can lead to an increase in the fin density and the exposed sites. The increase in fin density was observed previously when the thickness was increased from ~32 to ~64 nm (Figures 4f,g and S10b,c). A similar behavior can be expected in this scenario with the increase in thickness shown here.

On the other hand, an increase in film thickness for the H_2S process from ~8 to ~32 nm resulted in the reduction of the number of active sites/cm^2 from ~5.6 × 10^{15} to ~1.4 × 10^{15}. This reduction in the edge-site density can be understood from

DOI: 10.1021/acs.chemmater.9b01008
Chem. Mater. 2019, 31, 5104−5115

the evolution of the texture; layers that are not growing vertically (obliquely angled) will eventually be blocked by vertically growing layers (Figure S13). As a result, the top facet of the former layers containing the active sites will no longer be accessible for the adsorption of Cu in the electrolyte. Effectively, this leads to a reduction in the number of active sites per geometric area for Cu adsorption.

To summarize, with increasing film thickness, the WS_2 films exhibited a decrease in the number of active sites per geometric area in the case of the H_2S process, whereas an increase in the number of active sites per geometric area was observed for the $H_2 + H_2S$ process. The number of active sites determined for the WS_2 films grown using the H_2S process (5.6×10^{15}) was relatively higher than that reported by Voiry et al. (4.5×10^{14}–2×10^{15} sites/cm^2) for their chemically exfoliated, strained WS_2 nanosheets. However, this cannot be directly compared to our results as they utilized relatively thinner WS_2 films (~1 nm) with a different phase (1*T*) and larger lateral grain/flake size (100–800 nm). For ~1 nm thick WS_2 films grown in this study, the number of sites could not be estimated as the current density was too low to clearly identify the Cu stripping and UPD regimes. This suggested that the density of active sites was very low at this thickness and could be due to the fact that the film nanostructure was composed of a single or bilayer of horizontal basal planes (Figure 4d,g), which expose a significantly lower number of active sites than the out-of-plane structures.

Hydrogen Evolution Reaction (HER) Performance. The HER performance of WS_2 films was investigated using linear sweep voltammetry (LSV). Figure 5b shows a typical LSV plot for WS_2 films with comparable thicknesses and a bare glassy carbon substrate as the reference. From the LSV plot, it is evident that the WS_2 films exhibited significantly lower onset potential (~−200 mV) for HER than the reference bare glassy carbon substrate. Most importantly, the HER performance of WS_2 films was significantly better for the H_2S process than for the $H_2 + H_2S$ process in terms of the cathodic current density per geometric area (cm^2). This is in line with the Cu-UPD results (Figure 5a), where the number of active sites per geometric area (cm^2) was determined to be significantly higher for the H_2S process. Therefore, these data demonstrate the strong correlation between the HER performance and the number of active sites in our WS_2 films, which we control by varying our plasma settings.

To investigate the thickness dependence of the HER performance, the overpotential required to reach a current density of 10 mA/cm^2 (η_{10}) (from Figure 5a) was compared amongst our WS_2 films, as shown in Table 3. For the H_2S process, an increase in thickness from ~8 to ~32 nm resulted in an increase in η_{10} from −394 to −432 mV, indicating a degradation in the HER performance. This behavior can be predominantly attributed to a decrease in the number of active sites per geometric area with increased thickness, as shown in Figure 5a. Additionally, a thicker film can also offer a higher impedance for charge transfer, possibly adding to the degradation of the HER performance (Figure S14). An increase in resistance to charge transfer with increasing thickness has been previously reported for MoS_2.[29,47,48]

For the $H_2 + H_2S$ process, the increase in film thickness also led to a degradation in the HER performance (increase in η_{10} from −461 to −506 mV). However, this trend was not in accordance with the correlation between the number of active sites and film thickness shown in Figure 5a. This divergence can be largely attributed to the higher impedance of the thicker WS_2 films (Figure S14).

The HER activity is further illustrated by the Tafel slopes extracted from the Tafel plots in Figure 5c. A smaller Tafel slope is favorable for practical applications as a swift increase in HER activity can be expected with increasing overpotentials.[26,69] The calculated Tafel slopes were in the range of 110–180 mV/decade (Table 3), indicating that the Volmer reaction was the rate-determining step for HER.[29,37] The stability of the WS_2 electrocatalyst (~8 nm) synthesized using the H_2S process was investigated by recording the overpotential required to reach a current density of 5 mA/cm^2 (η_5) for over 25 h. As seen in Figure 5d, η_5 remained largely stable over time with the η_5 value ranging from ~−340 mV at the start of the stability test to ~370 mV after 25 h.

The ~8 nm WS_2 film grown using the H_2S process displayed efficient hydrogen evolution activity with a high current density of 83 mA/cm^2 at an overpotential of −0.63 mV versus RHE. However, the η_{10} value of −394 mV is relatively high when compared with other literature reports for WS_2.[28,30,37] The HER performance of our WS_2 films seems to be largely limited by the relatively high resistance to charge transfer.[28,37] This could be improved by enhancing the intrinsic conductivity of the WS_2 films by further fine-tuning the PEALD process (deposition temperature, plasma gas mixture, etc.) or by doping, which can be easily implemented with ALD.[70,71] We believe that the density of active sites can be further improved to enhance the HER performance. Employing high-surface-area 3D substrates and further optimizing process conditions such as plasma pressure, power, deposition temperature, etc., may be some of the possible ways to enhance the density of the active sites.

Table 3. Figures of Merit for the HER Performance of WS_2 Films with Varying Thicknesses Grown Using the H_2S and $H_2 + H_2S$ Processes

PEALD process	apparent film thickness (nm)	η_{10} (mV)	Tafel slope (mV/decade)
H_2S	~8	−394	122
	~32	−432	111
$H_2 + H_2S$	~8	−461	129
	~32	−506	177

CONCLUSIONS

By altering the co-reactant plasma gas composition from H_2S to $H_2 + H_2S$, the growth behavior and material properties of WS_2 (stoichiometry, crystallinity, and surface morphology) were tailored precisely using PEALD at a low temperature of 300 °C. The calculated adsorption energies by DFT indicated that the W precursor adsorption is stronger at the edge structure than at the basal plane. The abundantly adsorbed H atoms and S deficiency that result from the $H_2 + H_2S$ plasma further increase the adsorption rate and, consequently, lead to a higher GPC than in the case of the H_2S plasma. Adsorbed H atoms are transferred to the ligands of the W precursor and make a large contribution to the adsorption energy of the W precursor upon the inclusion of van der Waals interactions. These DFT results strongly correlate with our experimental findings. We demonstrated how PEALD can be used as a method to reliably nanoengineer the edge-site density and chemistry in our WS_2 films. The edge-enriched WS_2 electrocatalysts synthesized in this work showcased high HER

DOI: 10.1021/acs.chemmater.9b01008
Chem. Mater. 2019, 31, 5104–5115

efficiency. The predominantly edge-terminated and sulfur-rich WS_2 electrocatalysts synthesized using the H_2S process outperformed the tapered and sulfur-deficient electrocatalysts synthesized using the H_2 + H_2S process. Furthermore, the evaluation of the exposed active sites per geometric area through Cu-UPD enabled us to correlate the HER performance with the edge-site density. These results demonstrate how PEALD can be a reliable technique for the growth of edge-enriched WS_2 electrocatalysts and, potentially, a viable technique for growing similar 2D materials for relevant applications.

■ ASSOCIATED CONTENT

Supporting Information

The Supporting Information is available free of charge on the ACS Publications website at DOI: 10.1021/acs.chemmater.9b01008.

Impact of the plasma gas mixture on film properties, WS_2 PEALD saturation curves, XPS analysis, optical emission spectroscopy of the H_2S based plasmas, computational section: computational details, adsorption of the W precursor on the basal plane ({001} facet) and complementary calculations, TEM images and film properties of WS_2 films (t_{App} ∼ 64 nm) synthesized using the H_2 + H_2S process, copper UPD—evaluation of the number of active sites, surface morphology of WS_2 on different substrates, blocking of layers in WS_2 films, and electrochemical impedance spectroscopy data (PDF)

■ AUTHOR INFORMATION

Corresponding Author

*E-mail: a.a.bol@tue.nl.

ORCID

Shashank Balasubramanyam: 0000-0001-8728-9780
Mahdi Shirazi: 0000-0002-2497-3013
Wilhelmus M. M. Kessels: 0000-0002-7630-8226
Jan P. Hofmann: 0000-0002-5765-1096
Ageeth A. Bol: 0000-0002-1259-6265

Notes

The authors declare no competing financial interest.

■ ACKNOWLEDGMENTS

This work was supported by the European Research Council (Grant Agreement No. 648787-ALDof2DTMDs). The authors acknowledge the technical assistance offered by Jeroen van Gerwen and Cristian van Helvoirt. They also thank Harm Knoops and Tahsin Faraz for critical discussions and Yi Shu from Oxford Instruments for his assistance with the uniformity measurements. Solliance and the Dutch province of Noord-Brabant are acknowledged for funding the TEM facility.

■ REFERENCES

(1) Wang, Q. H.; Kalantar-Zadeh, K.; Kis, A.; Coleman, J. N.; Strano, M. S. Electronics and Optoelectronics of Two-Dimensional Transition Metal Dichalcogenides. *Nat. Nanotechnol.* **2012**, *7*, 699−712.

(2) Chhowalla, M.; Shin, H. S.; Eda, G.; Li, L.-J.; Loh, K. P.; Zhang, H. The Chemistry of Two-Dimensional Layered Transition Metal Dichalcogenide Nanosheets. *Nat. Chem.* **2013**, *5*, 263−275.

(3) Xu, M.; Liang, T.; Shi, M.; Chen, H. Graphene-Like Two-Dimensional Materials. *Chem. Rev.* **2013**, *113*, 3766−3798.

(4) Mak, K. F.; Shan, J. Photonics and Optoelectronics of 2D Semiconductor Transition Metal Dichalcogenides. *Nat. Photonics* **2016**, *10*, 216−226.

(5) Zhang, H. Ultrathin Two-Dimensional Nanomaterials. *ACS Nano* **2015**, *9*, 9451−9469.

(6) Mak, K. F.; Lee, C.; Hone, J.; Shan, J.; Heinz, T. F. Atomically Thin MoS_2: A New Direct-Gap Semiconductor. *Phys. Rev. Lett.* **2010**, *105*, No. 136805.

(7) Ganatra, R.; Zhang, Q. Few-Layer MoS_2: A Promising Layered Semiconductor. *ACS Nano* **2014**, *8*, 4074−4099.

(8) Albe, K.; Klein, A. Density-Functional-Theory Calculations of Electronic Band Structure of Single-Crystal and Single-Layer WS_2. *Phys. Rev. B* **2002**, *66*, No. 073413.

(9) Gutiérrez, H. R.; Perea-López, N.; Elías, A. L.; Berkdemir, A.; Wang, B.; Lv, R.; López-Urías, F.; Crespi, V. H.; Terrones, H.; Terrones, M. Extraordinary Room-Temperature Photoluminescence in Triangular WS_2 Monolayers. *Nano Lett.* **2013**, *13*, 3447−3454.

(10) Radisavljevic, B.; Radenovic, A.; Brivio, J.; Giacometti, V.; Kis, A. Single-Layer MoS_2 Transistors. *Nat. Nanotechnol.* **2011**, *6*, 147−150.

(11) Bao, W.; Cai, X.; Kim, D.; Sridhara, K.; Fuhrer, M. S. High Mobility Ambipolar MoS_2 Field-Effect Transistors: Substrate and Dielectric Effects. *Appl. Phys. Lett.* **2013**, *102*, No. 042104.

(12) Iqbal, M. W.; Iqbal, M. Z.; Khan, M. F.; Shehzad, M. A.; Seo, Y.; Park, J. H.; Hwang, C.; Eom, J. High-Mobility and Air-Stable Single-Layer WS_2 Field-Effect Transistors Sandwiched between Chemical Vapor Deposition-Grown Hexagonal BN Films. *Sci. Rep.* **2015**, *5*, No. 10699.

(13) Wu, D.; Li, X.; Luan, L.; Wu, X.; Li, W.; Yogeesh, M. N.; Ghosh, R.; Chu, Z.; Akinwande, D.; Niu, Q.; et al. Uncovering Edge States and Electrical Inhomogeneity in MoS_2 Field-Effect Transistors. *Proc. Natl. Acad. Sci. U.S.A.* **2016**, *113*, 8583−8588.

(14) Guo, M.; Yang, Y.; Leng, Y.; Wang, L.; Dong, H.; Liu, H.; Li, W. Edge Dominated Electronic Properties of MoS_2/Graphene Hybrid 2D Materials: Edge State, Electron Coupling and Work Function. *J. Mater. Chem. C* **2017**, *5*, 4845−4851.

(15) Yin, X.; Ye, Z.; Chenet, D. A.; Ye, Y.; O'Brien, K.; Hone, J. C.; Zhang, X. Edge Nonlinear Optics on a MoS_2 Atomic Monolayer. *Science* **2014**, *344*, 488−490.

(16) Lucking, M. C.; Bang, J.; Terrones, H.; Sun, Y.-Y.; Zhang, S. Multivalency-Induced Band Gap Opening at MoS_2 Edges. *Chem. Mater.* **2015**, *27*, 3326−3331.

(17) Lauritsen, J. V.; Nyberg, M.; Vang, R. T.; Bollinger, M. V.; Clausen, B. S.; Topsøe, H.; Jacobsen, K. W.; Lægsgaard, E.; Nørskov, J. K.; Besenbacher, F. Chemistry of One-Dimensional Metallic Edge States in MoS_2 Nanoclusters. *Nanotechnology* **2003**, *14*, 385−389.

(18) Deng, D.; Novoselov, K. S.; Fu, Q.; Zheng, N.; Tian, Z.; Bao, X. Catalysis with Two-Dimensional Materials and Their Heterostructures. *Nat. Nanotechnol.* **2016**, *11*, 218−230.

(19) Hinnemann, B.; Moses, P. G.; Bonde, J.; Jørgensen, K. P.; Nielsen, J. H.; Horch, S.; Chorkendorff, I.; Nørskov, J. K. Biomimetic Hydrogen Evolution: MoS_2 Nanoparticles as Catalyst for Hydrogen Evolution. *J. Am. Chem. Soc.* **2005**, *127*, 5308−5309.

(20) Jaramillo, T. F.; Jorgensen, K. P.; Bonde, J.; Nielsen, J. H.; Horch, S.; Chorkendorff, I. Identification of Active Edge Sites for Electrochemical H_2 Evolution from MoS_2 Nanocatalysts. *Science* **2007**, *317*, 100−102.

(21) Karunadasa, H. I.; Montalvo, E.; Sun, Y.; Majda, M.; Long, J. R.; Chang, C. J. A Molecular MoS_2 Edge Site Mimic for Catalytic Hydrogen Generation. *Science* **2012**, *335*, 698−702.

(22) Kibsgaard, J.; Jaramillo, T. F.; Besenbacher, F. Building an Appropriate Active-Site Motif into a Hydrogen-Evolution Catalyst with Thiomolybdate $[Mo_3S_{13}]^{2-}$ Clusters. *Nat. Chem.* **2014**, *6*, 248−253.

(23) Lukowski, M. A.; Daniel, A. S.; Meng, F.; Forticaux, A.; Li, L.; Jin, S. Enhanced Hydrogen Evolution Catalysis from Chemically Exfoliated Metallic MoS_2 Nanosheets. *J. Am. Chem. Soc.* **2013**, *135*, 10274−10277.

DOI: 10.1021/acs.chemmater.9b01008
Chem. Mater. 2019, 31, 5104−5115

(24) Benck, J. D.; Hellstern, T. R.; Kibsgaard, J.; Chakthranont, P.; Jaramillo, T. F. Catalyzing the Hydrogen Evolution Reaction (HER) with Molybdenum Sulfide Nanomaterials. *ACS Catal.* **2014**, *4*, 3957−3971.
(25) Yan, Y.; Xia, B.; Xu, Z.; Wang, X. Recent Development of Molybdenum Sulfides as Advanced Electrocatalysts for Hydrogen Evolution Reaction. *ACS Catal.* **2014**, *4*, 1693−1705.
(26) Wu, Z.; Fang, B.; Bonakdarpour, A.; Sun, A.; Wilkinson, D. P.; Wang, D. WS_2 Nanosheets as a Highly Efficient Electrocatalyst for Hydrogen Evolution Reaction. *Appl. Catal., B* **2012**, *125*, 59−66.
(27) Cheng, L.; Huang, W.; Gong, Q.; Liu, C.; Liu, Z.; Li, Y.; Dai, H. Ultrathin WS_2 Nanoflakes as a High-Performance Electrocatalyst for the Hydrogen Evolution Reaction. *Angew. Chem., Int. Ed.* **2014**, *53*, 7860−7863.
(28) Lukowski, M. A.; Daniel, A. S.; English, C. R.; Meng, F.; Forticaux, A.; Hamers, R. J.; Jin, S. Highly Active Hydrogen Evolution Catalysis from Metallic WS_2 Nanosheets. *Energy Environ. Sci.* **2014**, *7*, 2608−2613.
(29) Li, S.; Wang, S.; Salamone, M. M.; Robertson, A. W.; Nayak, S.; Kim, H.; Tsang, S. C. E.; Pasta, M.; Warner, J. H. Edge-Enriched 2D MoS_2 Thin Films Grown by Chemical Vapor Deposition for Enhanced Catalytic Performance. *ACS Catal.* **2017**, *7*, 877−886.
(30) Yang, Y.; Fei, H.; Ruan, G.; Li, Y.; Tour, J. M. Vertically Aligned WS_2 Nanosheets for Water Splitting. *Adv. Funct. Mater.* **2015**, *25*, 6199−6204.
(31) Yan, Y.; Xia, B.; Li, N.; Xu, Z.; Fisher, A.; Wang, X. Vertically Oriented MoS_2 and WS_2 Nanosheets Directly Grown on Carbon Cloth as Efficient and Stable 3-Dimensional Hydrogen-Evolving Cathodes. *J. Mater. Chem. A* **2015**, *3*, 131−135.
(32) Zhang, Y.; Shi, J.; Han, G.; Li, M.; Ji, Q.; Ma, D.; Zhang, Y.; Li, C.; Lang, X.; Zhang, Y.; et al. Chemical Vapor Deposition of Monolayer WS_2 Nanosheets on Au Foils toward Direct Application in Hydrogen Evolution. *Nano Res.* **2015**, *8*, 2881−2890.
(33) Voiry, D.; Yamaguchi, H.; Li, J.; Silva, R.; Alves, D. C. B.; Fujita, T.; Chen, M.; Asefa, T.; Shenoy, V. B.; Eda, G.; et al. Enhanced Catalytic Activity in Strained Chemically Exfoliated WS_2 Nanosheets for Hydrogen Evolution. *Nat. Mater.* **2013**, *12*, 850−855.
(34) Zhao, X.; Ma, X.; Sun, J.; Li, D.; Yang, X. Enhanced Catalytic Activities of Surfactant-Assisted Exfoliated WS_2 Nanodots for Hydrogen Evolution. *ACS Nano* **2016**, *10*, 2159−2166.
(35) Shang, X.; Rao, Y.; Lu, S. S.; Dong, B.; Zhang, L. M.; Liu, X. H.; Li, X.; Liu, Y. R.; Chai, Y. M.; Liu, C. G. Novel WS_2/WO_3 Heterostructured Nanosheets as Efficient Electrocatalyst for Hydrogen Evolution Reaction. *Mater. Chem. Phys.* **2017**, *197*, 123−128.
(36) Kong, D.; Wang, H.; Cha, J. J.; Pasta, M.; Koski, K. J.; Yao, J.; Cui, Y. Synthesis of MoS_2 and $MoSe_2$ Films with Vertically Aligned Layers. *Nano Lett.* **2013**, *13*, 1341−1347.
(37) Sun, C.; Zhang, J.; Ma, J.; Liu, P.; Gao, D.; Tao, K.; Xue, D. N-Doped WS_2 Nanosheets: A High-Performance Electrocatalyst for the Hydrogen Evolution Reaction. *J. Mater. Chem. A* **2016**, *4*, 11234−11238.
(38) Lin, J.; Peng, Z.; Wang, G.; Zakhidov, D.; Larios, E.; Yacaman, M. J.; Tour, J. M. Enhanced Electrocatalysis for Hydrogen Evolution Reactions from WS_2 Nanoribbons. *Adv. Energy Mater.* **2014**, *4*, No. 1301875.
(39) Wang, H.; Lu, Z.; Kong, D.; Sun, J.; Hymel, T. M.; Cui, Y. Electrochemical Tuning of MoS_2 Nanoparticles on Three-Dimensional Substrate for Efficient Hydrogen Evolution. *ACS Nano* **2014**, *8*, 4940−4947.
(40) Li, H.; Tsai, C.; Koh, A. L.; Cai, L.; Contryman, A. W.; Fragapane, A. H.; Zhao, J.; Han, H. S.; Manoharan, H. C.; Abild-Pedersen, F.; et al. Activating and Optimizing MoS_2 Basal Planes for Hydrogen Evolution through the Formation of Strained Sulphur Vacancies. *Nat. Mater.* **2016**, *15*, 48−53.
(41) Ye, G.; Gong, Y.; Lin, J.; Li, B.; He, Y.; Pantelides, S. T.; Zhou, W.; Vajtai, R.; Ajayan, P. M. Defects Engineered Monolayer MoS_2 for Improved Hydrogen Evolution Reaction. *Nano Lett.* **2016**, *16*, 1097−1103.
(42) Woods, J. M.; Jung, Y.; Xie, Y.; Liu, W.; Liu, Y.; Wang, H.; Cha, J. J. One-Step Synthesis of MoS_2/WS_2 Layered Heterostructures and Catalytic Activity of Defective Transition Metal Dichalcogenide Films. *ACS Nano* **2016**, *10*, 2004−2009.
(43) Wu, L.; van Hoof, A. J. F.; Dzade, N. Y.; Gao, L.; Richard, M.-I.; Friedrich, H.; De Leeuw, N. H.; Hensen, E. J. M.; Hofmann, J. P. Enhancing the Electrocatalytic Activity of 2H-WS_2 for Hydrogen Evolution via Defect Engineering. *Phys. Chem. Chem. Phys.* **2019**, *21*, 6071−6079.
(44) Ouyang, Y.; Ling, C.; Chen, Q.; Wang, Z.; Shi, L.; Wang, J. Activating Inert Basal Planes of MoS_2 for Hydrogen Evolution Reaction through the Formation of Different Intrinsic Defects. *Chem. Mater.* **2016**, *28*, 4390−4396.
(45) Chen, T.-Y.; Chang, Y.-H.; Hsu, C.-L.; Wei, K.-H.; Chiang, C.-Y.; Li, L.-J. Comparative Study on MoS_2 and WS_2 for Electrocatalytic Water Splitting. *Int. J. Hydrogen Energy* **2013**, *38*, 12302−12309.
(46) He, Q.; Wang, L.; Yin, K.; Luo, S. Vertically Aligned Ultrathin 1T-WS_2 Nanosheets Enhanced the Electrocatalytic Hydrogen Evolution. *Nanoscale Res. Lett.* **2018**, *13*, No. 167.
(47) Ho, T. A.; Bae, C.; Lee, S.; Kim, M.; Montero-Moreno, J. M.; Park, J. H.; Shin, H. Edge-On MoS_2 Thin Films by Atomic Layer Deposition for Understanding the Interplay between the Active Area and Hydrogen Evolution Reaction. *Chem. Mater.* **2017**, *29*, 7604−7614.
(48) Sharma, A.; Verheijen, M. A.; Wu, L.; Karwal, S.; Vandalon, V.; Knoops, H. C. M.; Sundaram, R. S.; Hofmann, J. P.; Kessels, W. M. M.; Bol, A. A. Low-Temperature Plasma-Enhanced Atomic Layer Deposition of 2-D MoS_2: Large Area, Thickness Control and Tuneable Morphology. *Nanoscale* **2018**, *10*, 8615−8627.
(49) Yeo, S.; Nandi, D. K.; Rahul, R.; Kim, T. H.; Shong, B.; Jang, Y.; Bae, J.-S.; Han, J. W.; Kim, S.-H.; Kim, H. Low-Temperature Direct Synthesis of High Quality WS_2 Thin Films by Plasma-Enhanced Atomic Layer Deposition for Energy Related Applications. *Appl. Surf. Sci.* **2018**, *459*, 596−605.
(50) Puurunen, R. L. Surface Chemistry of Atomic Layer Deposition: A Case Study for the Trimethylaluminum/Water Process. *J. Appl. Phys.* **2005**, *97*, No. 121301.
(51) George, S. M. Atomic Layer Deposition: An Overview. *Chem. Rev.* **2010**, *110*, 111−131.
(52) Biyikli, N.; Haider, A. Atomic Layer Deposition: An Enabling Technology for the Growth of Functional Nanoscale Semiconductors. *Semicond. Sci. Technol.* **2017**, *32*, No. 093002.
(53) Leskelä, M.; Ritala, M. Atomic Layer Deposition (ALD): From Precursors to Thin Film Structures. *Thin Solid Films* **2002**, *409*, 138−146.
(54) Profijt, H. B.; Potts, S. E.; van de Sanden, M. C. M.; Kessels, W. M. M. Plasma-Assisted Atomic Layer Deposition: Basics, Opportunities, and Challenges. *J. Vac. Sci. Technol., A* **2011**, *29*, No. 050801.
(55) Balasubramanyam, S.; Sharma, A.; Vandalon, V.; Knoops, H. C. M.; Kessels, W. M. M.; Bol, A. A. Plasma-Enhanced Atomic Layer Deposition of Tungsten Oxide Thin Films Using $(^tBuN)_2(Me_2N)_2W$ and O_2 Plasma. *J. Vac. Sci. Technol., A* **2018**, *36*, No. 01B103.
(56) Green, C. L.; Kucernak, A. Determination of the Platinum and Ruthenium Surface Areas in Platinum−Ruthenium Alloy Electrocatalysts by Underpotential Deposition of Copper. I. Unsupported Catalysts. *J. Phys. Chem. B* **2002**, *106*, 1036−1047.
(57) Kresse, G. Ab Initio Molecular Dynamics for Liquid Metals. *J. Non.-Cryst. Solids* **1995**, *192*−*193*, 222−229.
(58) Blöchl, P. E. Projector Augmented-Wave Method. *Phys. Rev. B* **1994**, *50*, 17953−17979.
(59) Perdew, J. P.; Burke, K.; Ernzerhof, M. Generalized Gradient Approximation Made Simple. *Phys. Rev. Lett.* **1996**, *77*, 3865−3868.
(60) Shirazi, M.; Kessels, W. M. M.; Bol, A. A. Initial Stage of Atomic Layer Deposition of 2D-MoS_2 on a SiO_2 Surface: A DFT Study. *Phys. Chem. Chem. Phys.* **2018**, *20*, 16861−16875.
(61) Shirazi, M.; Elliott, S. D. Multiple Proton Diffusion and Film Densification in Atomic Layer Deposition Modeled by Density Functional Theory. *Chem. Mater.* **2013**, *25*, 878−889.

DOI: 10.1021/acs.chemmater.9b01008
Chem. Mater. 2019, 31, 5104−5115

(62) Shirazi, M.; Elliott, S. D. Atomistic Kinetic Monte Carlo Study of Atomic Layer Deposition Derived from Density Functional Theory. *J. Comput. Chem.* **2014**, *35*, 244−259.
(63) Ritala, M.; Leskelä, M.; Dekker, J.; Mutsaers, C.; Soininen, P. J.; Skarp, J. Perfectly Conformal TiN and Al_2O_3 Films Deposited by Atomic Layer Deposition. *Chem. Vap. Deposition* **1999**, *5*, 7−9.
(64) Elers, K.-E.; Blomberg, T.; Peussa, M.; Aitchison, B.; Haukka, S.; Marcus, S. Film Uniformity in Atomic Layer Deposition. *Chem. Vap. Deposition* **2006**, *12*, 13−24.
(65) Schutte, W. J.; De Boer, J. L.; Jellinek, F. Crystal Structures of Tungsten Disulfide and Diselenide. *J. Solid State Chem.* **1987**, *70*, 207−209.
(66) Benck, J. D.; Chen, Z.; Kuritzky, L. Y.; Forman, A. J.; Jaramillo, T. F. Amorphous Molybdenum Sulfide Catalysts for Electrochemical Hydrogen Production: Insights into the Origin of Their Catalytic Activity. *ACS Catal.* **2012**, *2*, 1916−1923.
(67) Shin, S.; Jin, Z.; Kwon, D. H.; Bose, R.; Min, Y. S. High Turnover Frequency of Hydrogen Evolution Reaction on Amorphous MoS_2 Thin Film Directly Grown by Atomic Layer Deposition. *Langmuir* **2015**, *31*, 1196−1202.
(68) Zhang, X.; Luo, Z.; Yu, P.; Cai, Y.; Du, Y.; Wu, D.; Gao, S.; Tan, C.; Li, Z.; Ren, M.; et al. Lithiation-Induced Amorphization of Pd3P2S8 for Highly Efficient Hydrogen Evolution. *Nat. Catal.* **2018**, *1*, 460−468.
(69) Merki, D.; Hu, X. Recent Developments of Molybdenum and Tungsten Sulfides as Hydrogen Evolution Catalysts. *Energy Environ. Sci.* **2011**, *4*, 3878.
(70) Niemelä, J.-P.; Yamauchi, H.; Karppinen, M. Conducting Nb-Doped TiO_2 Thin Films Fabricated with an Atomic Layer Deposition Technique. *Thin Solid Films* **2014**, *551*, 19−22.
(71) Garcia-Alonso, D.; Potts, S. E.; van Helvoirt, C. A. A.; Verheijen, M. A.; Kessels, W. M. M. Atomic Layer Deposition of B-Doped ZnO Using Triisopropyl Borate as the Boron Precursor and Comparison with Al-Doped ZnO. *J. Mater. Chem. C* **2015**, *3*, 3095−3107.

DOI: 10.1021/acs.chemmater.9b01008
Chem. Mater. 2019, 31, 5104−5115